RSC Advances

PAPER

View Article Online
View Journal | View Issue

Cite this: *RSC Adv.*, 2026, **16**, 30601

Harnessing thermo-hydrogen coupling with palladium hydride nanoparticles for superior antitumor therapy

Xinyu Jiang,[a] Kun Li,[a] Penghui Zhao,[a] Dong Li,[*a] Jinwen Shi,[*a] Yan Zhou,[b] Fei Li,[*b] Bin Chen[*a] and Haiyan Chen*[cd]

Received 31st March 2026
Accepted 11th May 2026

DOI: 10.1039/d6ra02688e

rsc.li/rsc-advances

Photothermal nanomaterials have gained significant attention in cancer treatment due to their excellent photothermal conversion properties. However, photothermal therapy alone often results in incomplete tumor ablation. To improve therapeutic efficacy, we introduce a thermo-hydrogen coupled strategy using palladium hydride (PdH) nanoparticles that combine photothermal heating with hydrogen-driven oxidative stress modulation. PdH nanoparticles were synthesized *via* a chemical method and systematically characterized using transmission electron microscopy (TEM), X-ray diffraction (XRD), UV-Vis spectrophotometry, and thermos response measurements. The results demonstrated that PdH nanoparticles possess small size, high structural stability, good dispersibility, and a photothermal conversion efficiency of 61.9% at 100 μg mL^{-1}. Hydrogen release upon 532 nm laser irradiation was confirmed using methylene blue decolorization. *In vitro* studies demonstrated that under laser irradiation, PdH nanoparticles efficiently and stably released hydrogen, enhancing intracellular oxidative stress and leading to selective apoptosis in liver cancer cells while sparing normal liver cells. This effect resulted in an 82% cancer cell death rate, significantly surpassing that of Pd nanoparticles without hydrogen. These findings highlight the mechanistic advantage of thermo-hydrogen synergy and support PdH nanoparticles as a promising platform for controlled and selective cancer therapy.

1. Introduction

Hydrogen has long been recognized as a clean energy source,[1,2] but its biomedical potential only came to light in 2007 when Ohsawa *et al.* discovered hydrogen's selective antioxidant properties.[3] Since then, substantial evidence has shown that hydrogen can mitigate oxidative damage in neurodegenerative diseases (*i.e.* Alzheimer's disease, Parkinson's disease), as well as metabolic disorders (metabolic syndrome, diabetes, and mitochondrial disorders), by selectively neutralizing reactive oxygen species (ROS) without disturbing essential signaling radicals.[4] In addition to its antioxidant properties, hydrogen also exhibits excellent anti-inflammatory effects.[5] Given that chronic inflammation and ROS are major factors in cancer development, hydrogen's ability to suppress both inflammation and ROS suggests a potential role in cancer prevention and therapy.[6] Unlike conventional systemic hydrogen delivery methods including direct inhalation,[7] drinking hydrogen-saturated water[8] or hydrogen-saturated saline injection,[9] which suffer from poor targeting and rapid dispersion, nanotechnology offers a means to store, transport, and release H_2 in a controlled, localized manner. Due to their high specific surface area and ease of surface functionalization, nanocarriers can be engineered to unload gases in response to specific stimuli such as magnetic fields, electric fields, or lasers,[10–13] enabling on-demand hydrogen release at disease sites.

Palladium (Pd) nanoparticles have been demonstrated to not only efficiently load hydrogen,[14–17] but also commonly been used as photothermal conversion carriers in photothermal therapy (PTT), exhibiting excellent photothermal conversion capabilities.[18–21] PTT using Pd or other plasmonic nanomaterials has shown promise for noninvasive tumor ablation by laser-induced hyperthermia. However, PTT alone often cannot eradicate all cancer cells, and may induce inflammatory responses,[22,28,30] stimulating the regeneration of tumor cells and affect treatment efficacy.[22] Studies reported that Pd nanoparticles alone, while photothermally active, achieved low tumour cell lethality rate *in vitro*.[24] Therefore, incorporating anti-inflammatory strategies into photothermal tumor therapy is both necessary and effective.[23] However, previously reported

[a]*State Key Laboratory of Multiphase Flow in Power Engineering, Xi'an Jiaotong University, Xi'an 710049, China. E-mail: lidong@mail.xjtu.edu.cn*

[b]*The Key Laboratory of Biomedical Information Engineering of Ministry of Education, School of Life Science and Technology and Bioinspired Engineering and Biomechanics Center (BEBC), Xi'an Jiaotong University, Xi'an 710049, P. R. China. E-mail: feili@mail.xjtu.edu.cn*

[c]*Department of Geriatric General Surgery, The Second Affiliated Hospital of Xi'an Jiaotong University, Xi'an, 710004, China. E-mail: chenhaiyan0527@126.com*

[d]*Research Centre Laboratory, The Second Affiliated Hospital of Xi'an Jiaotong University, Xi'an, 710004, China. E-mail: chenhaiyan0527@126.com*

methods for synthesizing Pd nanoparticles are generally complex and often involve chemically hazardous reagents. For example, in some studies, rapid nucleation is achieved using a strong reducing agent ($NaBH_4$), followed by a seed-mediated growth strategy. Such approaches typically require multiple steps and stringent control over reaction conditions.[31] Furthermore, the solvothermal method for Pd nanoparticle synthesis generally requires a high-temperature and high-pressure autoclave, and is characterized by long reaction durations, typically up to approximately 20 h.[32,33]

Recent advances have begun exploring the thermo–hydrogen coupled therapeutic strategy, which have potential to mitigate the side effects of photothermal therapy while simultaneously enhancing its antitumor efficacy. Previous studies have applied thermo–hydrogen coupled therapy to the treatment of cervical cancer and achieved promising therapeutic outcomes.[17] For example, hydrogen-releasing nanomedicine such as Fe@CMC (carboxymethy cellulose)[30] have demonstrated selective killing of cancer cells. This dual mode mechanism is expected to amplify the therapeutic outcomes by increasing ROS generation in tumors while minimizing systemic exposure.

In this paper, we introduce PdH nanoparticles for tumor-targeted thermo-hydrogen therapy of cancer. PdH nanoparticles with a uniform size distribution were synthesized *via* a simple and cost-effective chemical route with a relatively short reaction time, thereby offering advantages in terms of scalability and reproducibility, and characterized their structure, hydrogen content, and photothermal performance. The results of the photothermal experiments indicated that PdH nanoparticles possess photothermal stability, making them suitable for prolonged and repeated laser irradiation, with high photothermal conversion efficiency. Controlled hydrogen release at temperatures below the biological damage threshold (60 °C) under laser stimulation was verified using a methylene blue assay. We then evaluated the *in vitro* therapeutic efficacy and mechanism of PdH on human liver cancer cells *versus* normal liver cells, including analyses of cell viability, live/dead staining, and intracellular ROS levels. The results show that under laser irradiation, PdH nanoparticles showed selectively killing of liver cancer cells while minimally affecting normal liver cells, effectively achieving cancer cell ablation while protecting normal cells. Pd nanoparticles alone were tested under identical cellular conditions, which confirmed that PdH nanoparticles exhibit markedly enhanced and selective cytotoxicity toward cancer cells, while Pd particles alone have limited effects. This synergistic effect of photothermal and hydrogen release capabilities of PdH points to a promising therapeutic strategy for cancer treatment, with potential for future *in vivo* translation.

2. Experimental methods

2.1 Synthesis of Pd and PdH nanoparticles

2.1.1 Preparation of Pd nanoparticles. Palladium nanoparticles were synthesized using a simple chemical synthesis method. Specifically, 57 mg of sodium tetrachloropalladate (Na_2PdCl_4), 106 mg of polyvinylpyrrolidone (PVP), 60 mg of ascorbic acid (AA), and 300 mg of potassium bromide (KBr) were dissolved in 11 mL of deionized water in a round-bottom flask. The solution was vigorously stirred until fully dissolved, resulting in a brownish-red solution. The round-bottom flask containing the reaction solution was then connected to a reflux condenser and secured on a magnetic heating stirrer. The mixture was stirred at 80 °C for 3 hours in an oil bath. During the reaction, the color of the solution gradually deepened, indicating the successful formation of Pd nanoparticles. After cooling to room temperature, the colloid was centrifuged using an Amicon ultrafiltration tube (100 kDa) at 3660 rpm for 30 minutes, followed by three rinses with deionized water. The purified palladium nanoparticles were resuspended in 10 mL of deionized water and stored at 4 °C in the dark.

2.1.2 Preparation of PdH nanoparticles. To load hydrogen into Pd, the above Pd nanoparticle dispersion was transferred into a 20 mL vial and sealed with a rubber stopper. One opening of the vial was connected to the outlet of a hydrogen generator, while the other was vented to the atmosphere with a needle to allow excess hydrogen to escape slowly. The hydrogen generator produced hydrogen at a rate of 500 mL min^{-1}. After passing hydrogen for 30 minutes, the hydrogenation of the Pd nanoparticles was completed, and the vial was sealed and wrapped in foil to prevent light exposure. The resulting hydrogenated palladium dispersion was transferred into an aluminum foil wrapped sealed centrifuge tube, and stored under refrigeration until use. The entire process was carried out at room temperature to ensure optimal hydrogen absorption (Fig. 1).

2.2 Characterization

Prior to characterization, the nanoparticle dispersions were purified by ultrafiltration and washed repeatedly with deionized water to remove free PVP and residual reactants as far as practicable (Fig. 2).

2.2.1 TEM testing. The morphology of the materials was characterized using transmission electron microscopy (TEM, Talos-F200X, Thermo Fisher): Appropriate concentrations of Pd and PdH nanoparticle solutions were dropped onto copper grids coated with a carbon film. After air-drying, the morphology was observed using a high-resolution TEM.

2.2.2 XRD analysis. The phase of the samples was determined using X-ray powder diffraction (XRD, D8 ADVANCE A25, BRUKER): Appropriate concentrations of Pd and PdH nanoparticle solutions were dropped onto glass slides and air-dried. Data were collected for the dried samples over a 0°–90° range using Cu Kα radiation ($\lambda = 1.54056$ Å) with a step size of 0.02°/s.

2.2.3 UV-Vis absorption spectroscopy. The UV-Vis-NIR absorption spectra of 30 μg mL^{-1} Pd and PdH nanoparticle solutions were measured using a UV-Vis spectrophotometer (PE Lambda950, PerkinElmer): At room temperature, 3 mL of Pd and PdH nanoparticle solutions were placed into quartz cuvettes with a 10 mm path length, and the absorbance was scanned over the 200–1100 nm range.

2.2.4 DLS and zeta potential characterization. The surface potential and particle size were determined using a Malvern particle size analyzer (Malvern Zetasizer Nano ZS90, Malvern Panalytical): At a constant temperature of 25 °C, appropriate

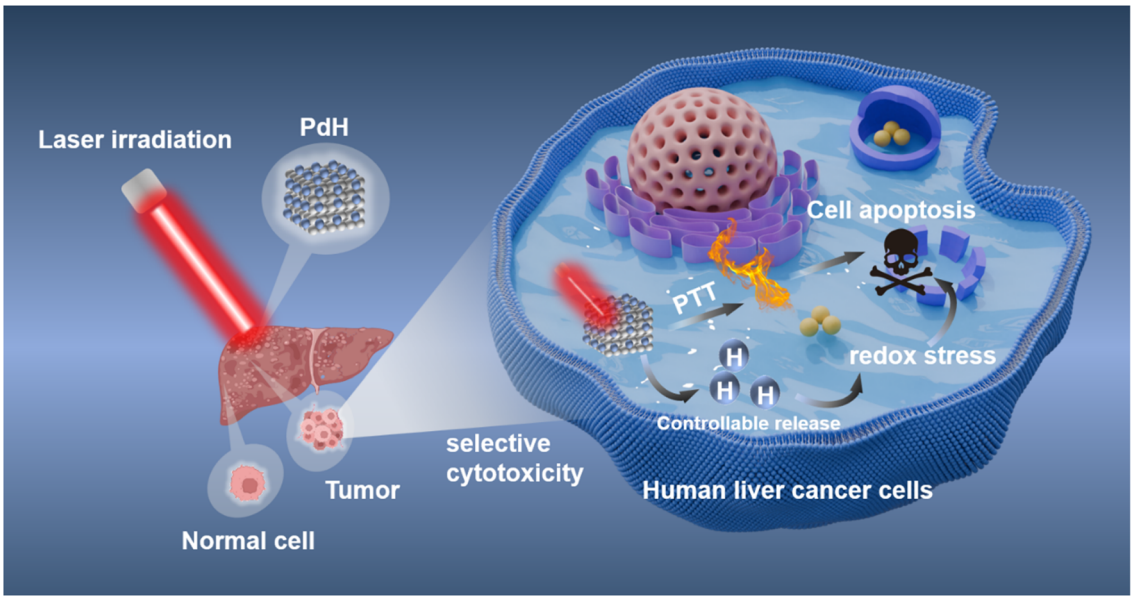

Fig. 1 Schematic illustration of the principle of hydrogen–thermal coupled therapy.

concentrations of Pd and PdH nanoparticle solutions were scanned 60 times, with three measurements taken. The average values were calculated, and a report was generated.

2.3 Stability of PdH nanoparticles

The obtained aqueous PdH solution was stored at low temperature under static conditions. For stability evaluation, PdH nanoparticles were stored in deionized water, PBS, and cell culture medium. The particle size and zeta potential of the same PdH nanoparticle solution were measured on days 1, 3, 5, 7, and 14.

2.4 Photothermal effect measurement

The photothermal performance of nanoparticles was evaluated under green laser irradiation (532 nm). In each test, 1 mL of the nanoparticle solution was placed in a quartz cuvette with a diameter of 10 mm, and then irradiated continuously for 5 minutes at a specific power density (*e.g.*, 1.0 W cm^{-2}). The selection of laser power density was based on the typical ranges reported in previous studies on Thermo-Hydrogen therapy.[6,17] After irradiation, allow the sample to cool naturally to ambient temperature. Throughout the test, the laser power density is calibrated and measured using a power meter, and the temperature change of the solution is monitored and recorded online every 20 seconds using an infrared thermal imaging camera (SC620, Teledyne FLIR). The photothermal conversion efficiency of the PdH nanoparticles is measured and calculated according to the method reported by Roper *et al.*[24]

For calculating the photothermal conversion efficiency under the given laser power and concentration, the following formula is typically used:

$$\eta_T = \frac{hS(T_{max} - T_r) - Q_d}{I(1 - 10^{-B_\lambda})} \quad (1)$$

where η_T is the photothermal conversion efficiency, T_{max} represents the maximum temperature of the PdH solution (°C), T_r is the ambient temperature (°C), I is the laser power (W), B_λ is the absorbance of the PdH solution at 532 nm, Q_d represents the rate of heat absorption of pure water under laser irradiation (J s^{-1}), h is the heat transfer coefficient of the system, S is the

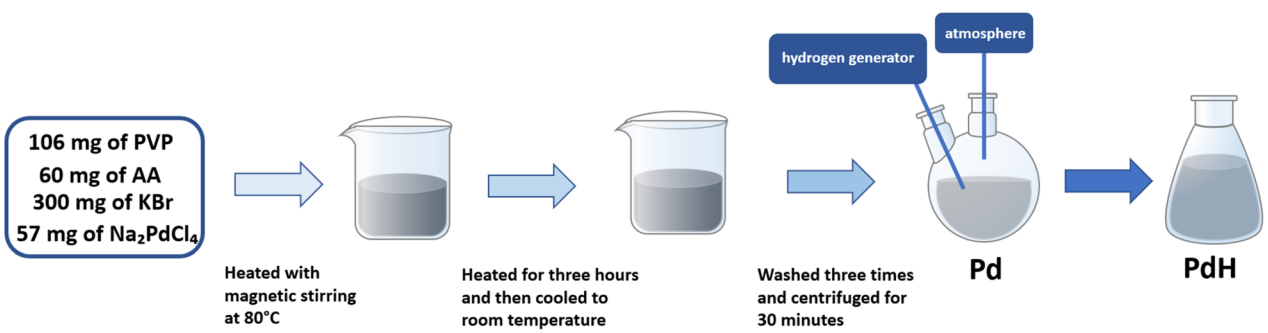

Fig. 2 Schematic of the synthesis process.

surface area of the quartz cuvette. The term hS (the product of the heat transfer coefficient and the surface area) can be calculated using eqn (2):

$$hS = \frac{m \times C_H}{\tau_m} \quad (2)$$

where m denotes the mass of the PdH solution (g), C_H indicates the specific heat capacity of water, τ_m refers to the time constant, which is determined using eqn (3):

$$t = -\tau_m \ln \theta = -\tau_m \ln\left(\frac{T - T_r}{T_{max} - T_r}\right) \quad (3)$$

where t denotes the time required for the solution to cool (s), θ represents the thermal driving constant, T is the temperature at time t (°C), T_{max} is the maximum temperature of the PdH solution (°C), T_r is the ambient temperature (°C), The value of τ_m is obtained through linear fitting.

2.5 Hydrogen release detection

To assess hydrogen release from PdH, we adopted a methylene blue (MB) reduction assay. Methylene blue is reduced and decolorized in the presence of hydrogen under certain conditions, serving as an indirect indicator of H_2 release. Briefly, 3 mL of methylene blue solutions at concentrations of 1, 1.5, 3, 5, 8, and 10 μg mL^{-1} were placed in quartz cuvettes with a light path width of 10 mm. Their absorbance at 664 nm was measured, and a linear calibration plot of absorbance *vs.* MB concentration was obtained. For the release experiment, the experiment was divided into two groups: (i) fresh PdH solution subjected to 532 nm laser (1.0 W cm^{-2}) irradiation, and (ii) PdH solution stored for 14 days in a cool, light-protected environment and subsequently subjected to 532 nm laser irradiation (1.0 W cm^{-2}). The total measurement duration for each group was 60 min, with measurements conducted at 0, 3, 5, 10, 20, 30, 40, and 60 min. In the mixed solution of PdH nanoparticles and methylene blue, the concentration of PdH nanoparticles was 3 μg mL^{-1}, and the concentration of methylene blue was 5 μg mL^{-1}. The total volume of the mixed solution was 3 mL.

To further distinguish PdH from Pd, *in situ* electrochemical measurements were conducted based on the catalytic activity of platinum toward the hydrogen oxidation reaction.[34] A microdisk electrode and a wire electrode were used as the working and counter electrodes, respectively, with an Ag/AgCl electrode as the reference, forming a standard three-electrode system. The measurements were performed in a water bath under varying temperature conditions. Prior to testing, the solution and reactor were purged with N_2 for 10 min to remove dissolved O_2, and a continuous low flow of N_2 was maintained over the solution throughout the experiment.

2.6 Cell lines and culture

Human liver cells (LO2), human liver cancer cells (HepG2), and human liver cancer cells (SMMC-7721) were seeded separately in a 96-well plate. Cells were cultured in high-glucose Dulbecco's Modified Eagle Medium (DMEM) supplemented with 10% fetal bovine serum (FBS), 100 U mL^{-1} penicillin, and 100 μg mL^{-1} streptomycin. All cells were maintained in a humidified incubator at 37 °C with 5% CO_2 and 90% relative humidity. Cells and their subtypes were detached using 0.25% (w/v) trypsin solution. LO2, HepG2, and SMMC-7721 were purchased from National Collection of Authenticated Cell Cultures, Chinese Academy of Sciences. Fetal bovine serum was purchased from Thermo Fisher Scientific.

2.7 *In vitro* cytotoxicity assay

PdH nanoparticles of different concentrations (0, 25, 50, 100, 150, 200, 400 μg mL^{-1}) were used in laser-irradiated and non-irradiated groups. For laser-irradiated group, cells were exposed to a 532 nm laser at 1.0 W cm^{-2} for 5 minutes per well, while the non-irradiated group receives no treatment. Under the same conditions, control experiments were performed using Pd nanoparticles. After treatment, cells were washed with sterile PBS buffer for three times (150 μL per wash) to remove nanoparticles, and then incubated with fresh medium. Cell viability is then assessed using a CCK-8 assay kit. After adding CCK-8 solution at a concentration of 5 mg L^{-1} and incubating for 2 hours, the absorbance at 450 nm was recorded using a microplate reader. Cell viability was calculated relative to untreated controls.

2.8 Live/dead cell staining experiment and intracellular ROS detection

A calcein-AM/PI live/dead double-staining assay was used to evaluate cell viability. Normal human liver cells (LO2) and human liver cancer cell lines (HepG2 and SMMC-7721) were treated with three representative concentrations of PdH (0, 50, and 150 μg mL^{-1}) or Pd particles at the same concentrations. For each concentration, cells were divided into non-irradiated and irradiated groups. The irradiated groups were exposed to a 532 nm laser at a power density of 1.0 W cm^{-2} for 5 minutes. Cell viability was determined based on fluorescence imaging. Apoptotic cells exhibit red fluorescence, whereas non-apoptotic cells show green fluorescence. The proportion and intensity of red *versus* green fluorescence in each group reflects cell viability.

Cellular reactive oxygen species (ROS) levels were measured using the DCFH-DA fluorescent probe. Normal human liver cells (LO2) and human liver cancer cell lines (HepG2 and SMMC-7721) were treated with three representative concentrations of PdH (0, 50, and 150 μg mL^{-1}). For each concentration, cells were divided into non-irradiated and irradiated groups. The irradiated groups were exposed to a 532 nm laser at a power density of 1.0 W cm^{-2} for 5 minutes per well. Fluorescence images were acquired under identical microscope settings for all groups. The mean fluorescence intensity was quantified using a Leica SP8 Confocal Microscope in combination with LAS X software. After background subtraction, the mean fluorescence intensity (MFI) was calculated as the arithmetic mean of valid pixel gray values within the selected ROI. The results are reported as relative DCF fluorescence intensity.

2.9 Statistical analysis

The data were expressed through three independent experiments, and the statistical analyses were performed. Statistical significance was shown by $*p < 0.05$, $**p < 0.01$, and $***p < 0.001$, respectively.

3. Result and discussion

3.1 Characterization of Pd and PdH nanoparticles

The morphology of chemically synthesized Pd nanoparticles and PdH nanoparticles was characterized using TEM, with the results shown in Fig. 3A and B, respectively. The Pd nanoparticles are cubic in shape with uniform size around 30 nm. The PVP capping agent effectively controlled particle morphology, resulting in good dispersibility of Pd particles (see Fig. 3A). In comparison, the PdH nanoparticles (Fig. 3B) retained the cubic morphology and excellent size distribution as Pd, with no observable aggregation. The similarity in size and shape indicates that the hydrogen-loading process did not cause particle sintering or shape alteration. DLS measurements further showed that both the Pd and PdH nanoparticles have sizes in the range of 10–100 nm, with an average size of 30 nm. The size of the PdH particles is slightly larger than that of the Pd particles, indicating effective hydrogen loading in the PdH particles. As shown in Fig. 3D, the zeta potential of the Pd and PdH nanoparticles are essentially equal in magnitude but opposite in sign. Pd nanoparticles were positively charged (+18 mV) due to the absence of hydrogen atoms in the lattice that prevent electron donation, thereby hindering the accumulation of electrons on the surface, whereas PdH exhibited a negative potential (−19 mV) the charge inversion upon hydrogenation provides further evidence that hydrogen atoms were incorporated. Such zeta potential shift confirms the successful hydrogenation of the palladium particles.

To analyse the stability of PdH nanoparticles, we monitored PdH dispersions over time. PdH nanoparticle were stored in deionized water, PBS solution, and cell culture medium, and the particle size and zeta potential were measured on day 1, 3, 5, 7, and day 14. The particle size and zeta potential of the PdH nanoparticles remained essentially unchanged over two weeks, as shown in Fig. 3E and F. This indicates excellent structural stability of the PdH nanoparticles in physiological-like conditions, with minimal particle aggregation or hydrogen loss over time. Such stability of PdH materials is critical for biomedical applications, ensuring that PdH can maintain stability to the target sites with its H cargo over a certain period.

The phases of Pd and PdH nanoparticles were revealed by X-ray diffraction (XRD) analysis (Fig. 3G). Both the XRD curves of Pd and PdH nanoparticles exhibit four distinct peaks in the diffraction angle range of 20–90°, indicating that both have a cubic crystal structure. The relevant parameters of PdH nanoparticles at the peak are higher than those of Pd nanoparticles at their respective peak. This suggests that polyvinylpyrrolidone (PVP) effectively modifies the nanoparticles and that hydrogen atoms have been incorporated into the lattice structure of the palladium nanoparticles.

The UV-Vis absorption spectra of Pd and PdH nanoparticles are shown in Fig. 3H. The absorption curves for both Pd and PdH show a decreasing trend with increasing wavelength toward NIR range. The absorbance of both materials is quite similar in the UV region, but differs in the visible and near-infrared regions. In the near-infrared absorption region, PdH exhibits stronger absorbance. Around 532 nm, PdH also shows higher absorbance than Pd, further confirming the successful hydrogen loading of the Pd nanoparticles. This is consistent

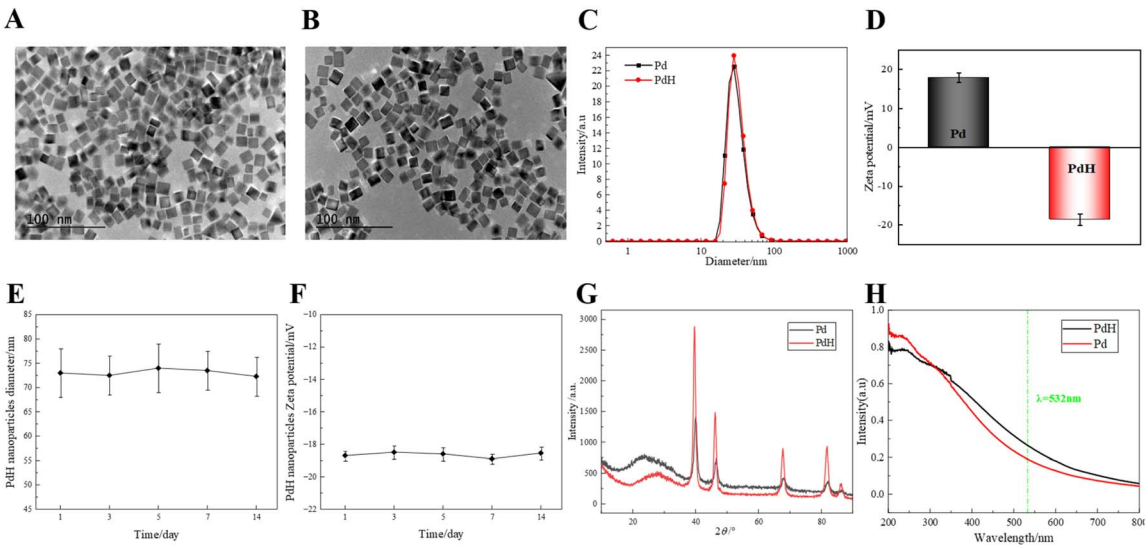

Fig. 3 Characterization of PdH and Pd nanoparticles. (A) TEM images of Pd nanoparticles (Scale bar: 100 nm); (B) TEM images of PdH nanoparticles (Scale bar: 100 nm); (C) size distribution of PdH and Pd nanoparticles; (D) zeta potential diagrams of Pd and PdH; (E) the particle sizes of PdH nanoparticles dispersed in water on days 1, 3, 5, 7, and 14; (F) zeta potential of PdH nanoparticles dispersed in water on days 1, 3, 5, 7, and 14; (G) X-ray diffraction (XRD) patterns of Pd and PdH nanoparticles; (H) the UV-Vis absorption spectra of Pd and PdH nanoparticles.

with prior reports that the absorbance of PdH is higher than that of Pd near 532 nm.[17]

The high-angle annular dark-field (HAADF) images and energy-dispersive X-ray spectroscopy (EDS) spectra of Pd and PdH nanoparticles were performed to verify the distribution of elements as shown in Fig. 4. From the HAADF images of Pd and PdH nanoparticles (Fig. 4A and B), it can be observed that Pd elements are evenly distributed within the cubic particles. Similarly, EDS spectra of both materials (Fig. 4C and D) displayed two characteristic Pd peaks with little difference between them. Combining these results, it can be concluded that the distribution of Pd elements in both Pd and PdH nanoparticles is uniform, and they differ mainly in the presence of lattice-stored hydrogen.

3.2 Photothermal effect of PdH nanoparticles

Due to the excellent light absorption capacity and aqueous dispersibility of PdH nanoparticles, we next examined the photothermal conversion performance of PdH nanoparticles under 532 nm laser irradiation. Fig. 5A compares the photothermal conversion properties of PdH *vs.* Pd and water under the same laser power density and concentration. With increasing laser irradiation time, both PdH and Pd nanoparticles exhibited gradually temperature elevation, with PdH showing a slightly higher temperature rise than Pd nanoparticles. In contrast, deionized water showed only a minor temperature increase by 4.2 °C, indicating that the laser alone causes negligible heating of the solvent, and the temperature rise in PdH solutions is due to nanoparticles' photothermal effect. This demonstrates that PdH nanoparticles possess excellent photothermal conversion capabilities.

Subsequently, we explored the effects of PdH nanoparticle concentration and laser irradiation power density on the material's heating capacity. As shown in Fig. 5B, at a constant PdH concentration, ramping the laser power from 0.25 to 1.5 W cm^{-2} caused the increase of heating rate and final temperature. Similarly, at a fixed laser power, increasing material concentration, the solution temperature rose rapidly, ranging from 5 °C to 50 °C (Fig. 5C). These trends demonstrate that PdH-mediated photothermal heating can be tuned by adjusting particle dosage and laser intensity, the higher the material concentration and the greater the laser energy, the faster the heating rate and the higher the final temperature. Infrared thermal imaging provides a direct visualization of the superior photothermal conversion performance of the PdH nanoparticles. As shown in Fig. 5C, under the same 532 nm irradiation, the PdH suspension shows a bright thermal profile, whereas water remains dark. As shown in Fig. 5E and F, the temperature variation curve for PdH nanoparticles demonstrates a significant temperature increase. After laser irradiation, the temperature of the PdH nanoparticle solution rose from ambient temperature (25.1 °C) to 45.8 °C, with a temperature difference of 20.7 °C. And the system time constant (τ_m) of the PdH nanoparticles was determined to be 411.958 s. According to the previously mentioned photothermal conversion efficiency formula, the photothermal conversion efficiency of the PdH nanoparticles was determined to be 61.9%, far higher than the PdH's photothermal conversion efficiency of 36% reported by Chen *et al.*[25]

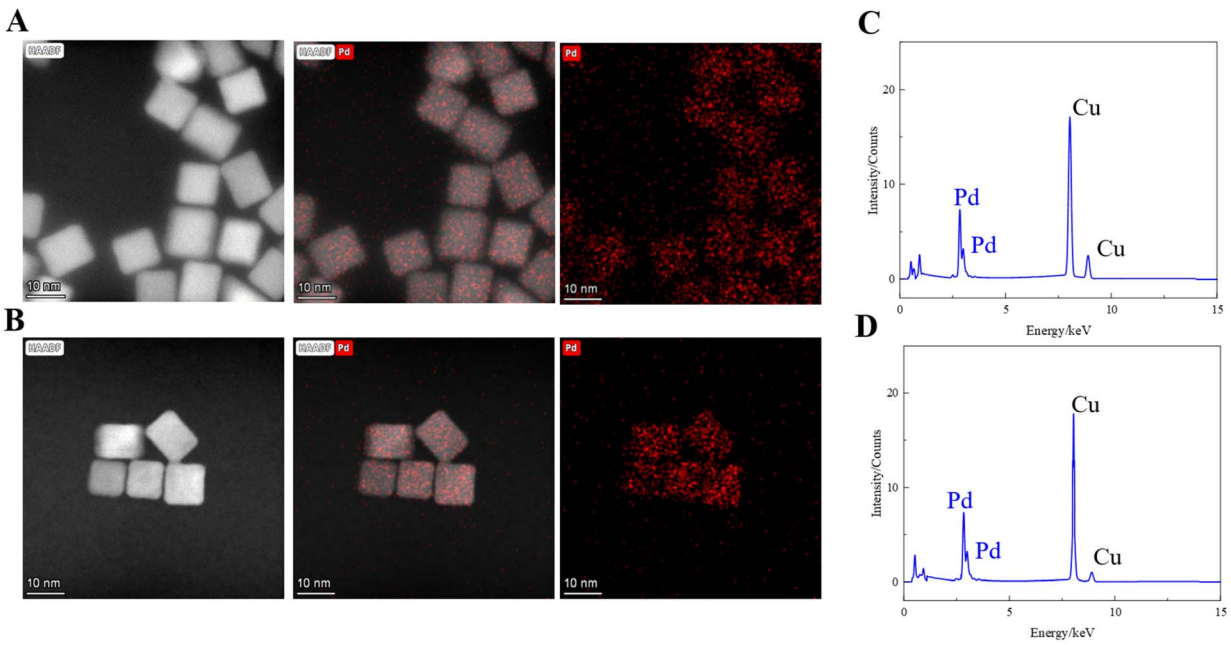

Fig. 4 The high-angle annular dark-field (HAADF) images and energy-dispersive X-ray spectroscopy (EDS) spectra of Pd and PdH nanoparticles. (A) HAADF image of Pd, right: external structure; left: internal elemental distribution; middle: merged image of left and right; (B) HAADF image of PdH, right: external structure; left: internal elemental distribution; middle: merged image of left and right; (C) EDS spectrum of Pd; (D) EDS spectrum of PdH.

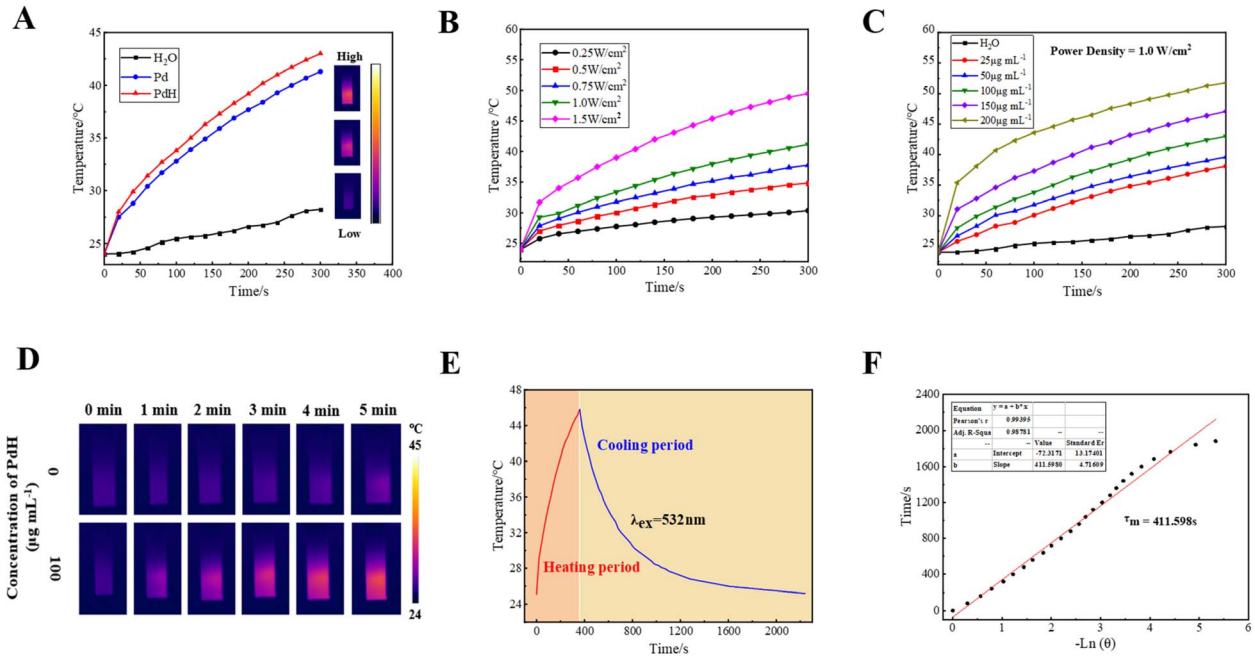

Fig. 5 Photothermal Effect of PdH nanoparticles. (A) Photothermal heating curves of Pd nanoparticles, PdH nanoparticles, and water under the same concentration and power density conditions (concentration: 100 μg mL^{-1}, power density: 1 W cm^{-2}); (B) temperature rise curves of PdH aqueous solution (50 μg mL^{-1}) with the same concentration and volume under different power levels (0.25, 0.5, 0.75, 1.0, and 1.5 W cm^{-2}); (C) temperature rise curves of PdH aqueous solution with varying concentrations (0, 25, 50, 100, 150, and 200 μg mL^{-1}) under the same power density (1 W cm^{-2}) and volume conditions; (D) photothermal heating curves of PdH nanoparticles (100 μg mL^{-1}) and water under the same power density conditions. (E) Photothermal heating curve of PdH nanoparticles (concentration: 100 μg mL^{-1}, power density: 1 W cm^{-2}); (F) the linear fitting curve of the natural logarithm of the thermal driving force *versus* time during the cooling process.

3.3 Thermo-hydrogen release from PdH nanoparticles

To investigate whether laser irradiation triggers the hydrogen release from the nanoparticles, we employed a methylene blue–based analytical method, in which methylene blue can be reduced by hydrogen-derived compounds. As shown in Fig. 6A, the absorbance value at the absorption peak of 664 nm was used to establish the standard curve equation relating methylene blue concentration to absorbance. Based on the relationship between concentration and peak intensity, the standard curve equation was created for reference in subsequent experiments (Fig. 6B).[26,27]

As shown in Fig. 7A and B, the fresh PdH nanoparticles and the PdH nanoparticles stored for 14 days under cool and light-protected conditions exhibited highly consistent absorption spectral characteristics and similar absorbance variations at 664 nm, indicating the excellent hydrogen storage stability of the material. Furthermore, the quantitative results presented in

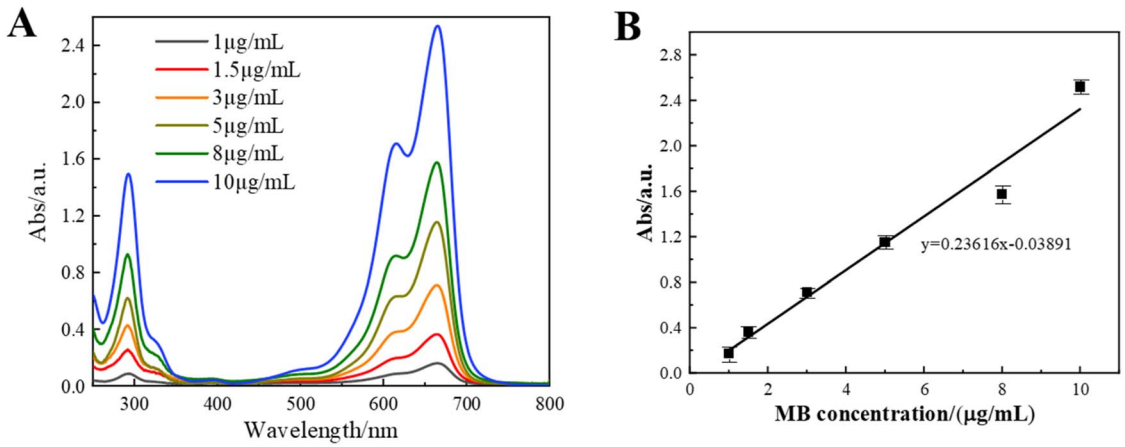

Fig. 6 Spectral absorption characteristics of methylene blue solutions. (A) UV-Vis absorption spectra of methylene blue solutions; (B) The equation of the standard curve relating concentration to absorbance at 664 nm for methylene blue solutions.

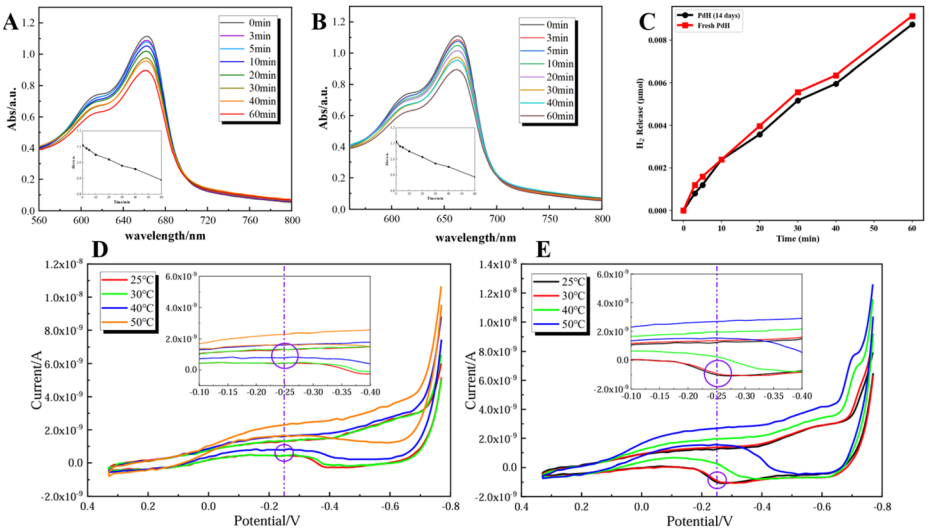

Fig. 7 Photohydrogen release performance of PdH nanoparticles. (A) UV-Vis absorption spectra of the mixed solution containing fresh PdH nanoparticles and methylene blue (MB) under different irradiation times. (B) UV-Vis absorption spectra of the mixed solution containing PdH nanoparticles stored for 14 days and MB under different irradiation times. (C) Quantitative analysis of hydrogen release from different PdH nanoparticle groups. (D) Cyclic voltammograms of the Pd solution. (E) Cyclic voltammograms of the PdH solution.

Fig. 7C revealed that the final hydrogen release amounts of the two groups were 0.00913 μmol and 0.00874 μmol, respectively, further demonstrating that the PdH nanoparticles maintained stable hydrogen release performance even after long-term storage.

To further verify the hydrogen loading capability of PdH, *in situ* electrochemical measurements were conducted. As shown in Fig. 7D and E, the cyclic voltammograms of Pd and PdH solutions are presented, respectively. In comparison, a distinct oxidation peak appears at −0.25 V in the PdH solution, whereas no corresponding peak is observed in the Pd solution. This result indicates the successful incorporation of hydrogen in the PdH nanoparticles.

By comparing the results from the experimental groups, it can be concluded that PdH is an excellent hydrogen storage material. The hydrogen it carries can be released in a controlled manner under laser irradiation at temperatures below the biological damage threshold (60 °C). This property makes PdH a promising candidate for biomedical applications that require safe and effective hydrogen release at specific temperatures.

3.4 Thermo-hydrogen coupling enhanced cancer therapy with PdH nanoparticles: comparative evaluation with Pd nanoparticles

We first assessed the cellular compatibility of PdH nanoparticles on normal liver cells (LO2) *vs.* liver cancer cells (HepG2 and SMMC-7721). The results are shown in Fig. 8A–C. It can be observed that without laser irradiation, PdH nanoparticles do not exhibit significant toxicity toward normal liver cells or cancer cells across the tested concentrations. Under 532 nm laser irradiation, as shown in Fig. 8A, when the PdH concentration is 100–150 μg mL^{-1}, LO2 cells maintain relatively high viability, with approximately 60% viability still retained at 150 μg mL^{-1}. A noticeable decline in LO2 viability (to 26%) is only observed when the PdH concentration reaches 200 μg mL^{-1}. In other words, moderate levels of PdH plus photothermal treatment caused little harm to normal cells. In contrast, human hepatocellular carcinoma cells SMMC-7721 and HepG2 were much more susceptible to laser irradiation and PdH treatment. At just 50 μg mL^{-1} PdH with laser, both cancer lines began showing reduced viability. At 100 μg mL^{-1}, the viability of both liver cancer cell lines drops significantly, falling to below 30%. When the concentration reaches 200 μg mL^{-1}, cell viability decreases to below 10%, with nearly all cancer cells being killed. These results suggest that under laser irradiation, PdH nanoparticles can selectively kill liver cancer cells while having a relatively minor effect on normal liver cells. Notably, 200 μg mL^{-1} PdH with laser achieved >90% killing of SMMC-7721 and >70% killing of HepG2 cancer cells.

To verify that this effect indeed arises from the hydrogen-carrying capacity of PdH, we performed parallel experiments with Pd nanoparticles under the same laser conditions. As shown in Fig. 8D–F, under laser irradiation, Pd nanoparticles exhibited limited cytotoxicity against SMMC-7721 and HepG2 cancer cells. Even at a high concentration of 200 μg mL^{-1} under laser exposure, SMMC-7721 cells retained around 40% viability, and HepG2 cells exhibited as high as 80% viability. LO2 cells maintained relatively high viability at concentrations below 100 μg mL^{-1}. However, when the concentration increased to 150 μg mL^{-1}, cell viability dropped to approximately 40%. This difference between Pd and PdH confirms the importance of hydrogen component in thermo-hydrogen coupling enhanced cancer therapy.

We then conducted live/dead cell staining experiment after treatments (Fig. 9). Based on the results from the photothermal experiments, three concentrations of PdH (0, 50, and 150 μg mL^{-1}) were selected. For LO2 cells, regardless of laser

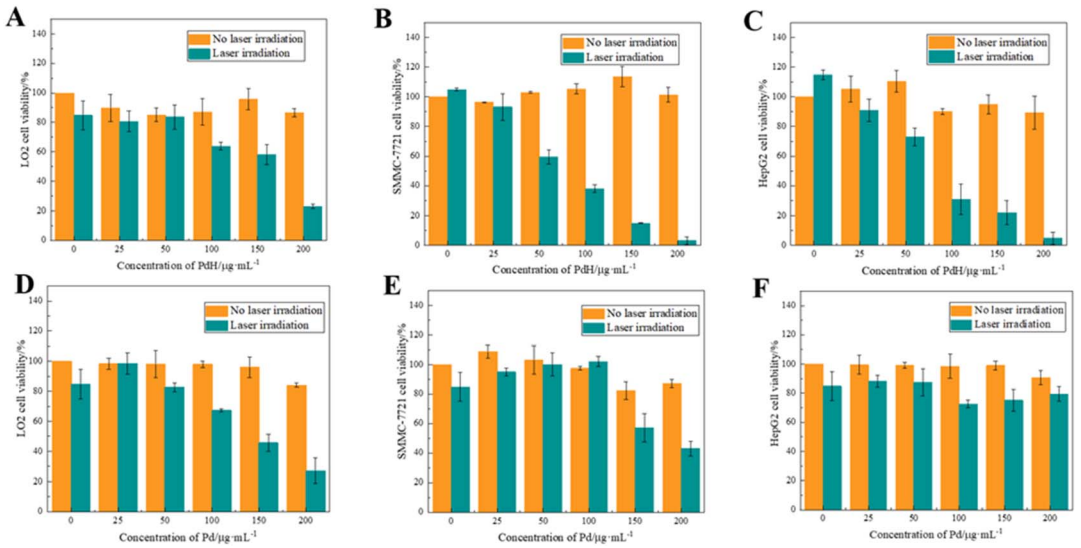

Fig. 8 Cellular compatibility testing. (A) Cell viability of LO2 cells, (B) cell viability of SMMC-7721 cells, (C) cell viability of HepG2 cells at different PdH concentration; (D) cell viability of LO2 cells, (E) cell viability of SMMC-7721 cells, (F) cell viability of HepG2 cells at different Pd concentration.

irradiation or the presence of PdH, the fluorescence is almost entirely green, indicating that the cells are predominantly alive. From the quantitative results (Fig. 9B), it can be observed that the survival rate of LO2 cells remained nearly 100% in all groups, which is consistent with the viability assay showing minimal impact on normal cells at the tested PdH concentrations.

For HepG2 cells, it can be observed that in the absence of laser irradiation, the fluorescence is almost entirely green, indicating that the presence of PdH alone has no significant effect on the survival of HepG2 cells. However, in Fig. 9A and C, under laser irradiation but without PdH, a few red fluorescence signals appear, indicating a small number of dead cells. When the PdH concentration is 50 μg mL^{-1}, some dead cells were observed, and the proportion of live cells in the staining results for HepG2 cells decreases to 44%. And at 150 μg mL^{-1}, a substantial number of dead cells are present, and the proportion of live cells in the staining results drops to 18% for HepG2 cells. This demonstrates that the combined action of the laser and PdH can effectively kill HepG2 cells, and this dose-dependent effect of cell killing matches the CCK-8 viability results. Similarly, according to the live/dead cell staining results for SMMC-7721 cells in Fig. 9A and D, the therapeutic effect is positively correlated with the material concentration. At 150 μg

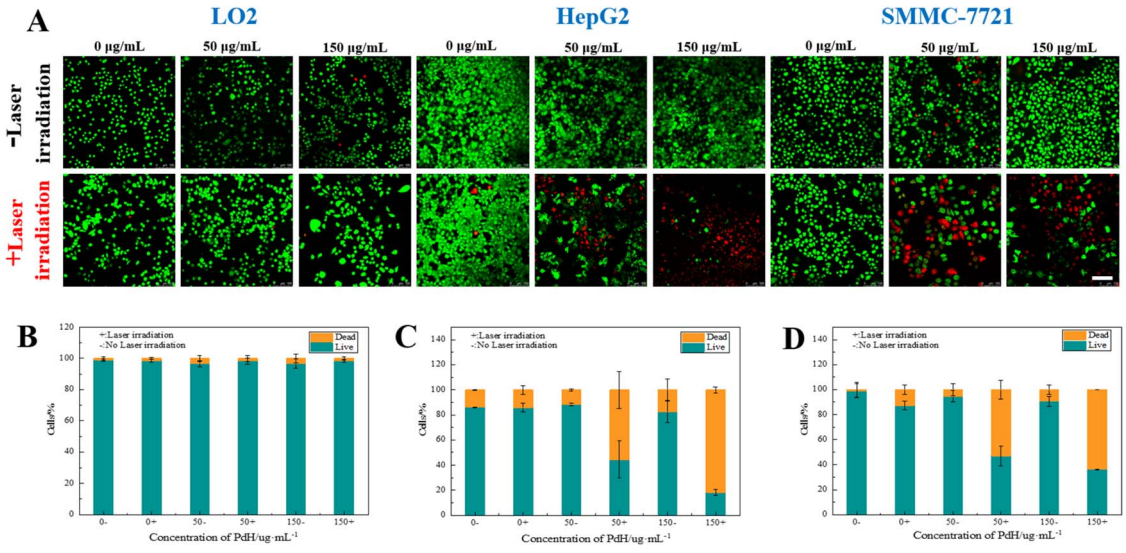

Fig. 9 Live/dead cell staining results of three types of cells under different conditions using PdH nanoparticles. (A) Fluorescence images of live/dead staining of human liver cells and liver cancer cells treated with different concentrations of PdH with or without 532 nm light irradiation (Scale = 100 μm); (B–D) quantification results of green/red fluorescence for LO2 cells, HepG2 cells and SMMC-7721 cells at different PdH concentrations. The data are shown as mean SD (n = 3).

mL^{-1}, the PdH nanoparticles can achieve an 82% killing effect on SMMC-7721 cells, significantly enhancing the therapeutic efficacy.

For comparison, live/dead staining with Pd were also performed as shown in Fig. 10. As shown in Fig. 10A, Pd nanoparticles exhibited no significant cytotoxic effect on normal cells or cancer cells at any concentrations, regardless of laser irradiation. The quantitative analyses in Fig. 10B to D further showed that the minimum cell viability for both cancer cell lines remained around 80% even at 150 μg mL^{-1}. Above all, the cell viability assay and the live/dead cell staining in Fig. 9 and 10 reveal that the hydrogenation therapy utilizing PdH nanoparticles achieves a synergistic effect by combining hydrogen and photothermal therapy. It should be noted that CCK-8 and live/dead cell staining reflect different cellular endpoints. CCK-8 mainly measures dehydrogenase-related metabolic activity, whereas live/dead staining reflects membrane integrity at the staining time point. Cells show reduced metabolic activity after Pd-mediated photothermal stress while retaining membrane integrity during live/dead staining. These results further underscore the superior efficacy and therapeutic potential of the thermal hydrogen-coupled treatment. While the photothermal effect ablates cancer cells, the hydrogen atmosphere selectively kills tumor cells and protects normal cells from oxidative stress, enabling selective cytotoxicity against cancer cells.[6]

3.5 Effect of PdH nanoparticles on intracellular reactive oxygen species

To elucidate the mechanism behind the selective cancer cell killing by thermo-hydrogen coupled therapy, we then examined intracellular ROS levels in treated cells. Based on the results of the cell compatibility experiments, we selected three concentrations of PdH/Pd nanoparticles: 0, 50, and 150 μg mL^{-1}, and a total of six groups were studied to investigate the effects of PdH/Pd nanoparticles and thermal hydrogen coupling on intracellular ROS levels. As shown in Fig. 11A and B, the intracellular ROS levels of LO2 cells are very low in the absence of laser irradiation, reflecting the normal metabolic ROS content of the cells. Interestingly, when PdH nanoparticles were present, LO2 cells did not accumulate excess ROS. When subjected to laser irradiation, the fluorescence intensity shows a slight increase, indicating a minor rise in ROS levels in LO2 cells (Fig. 11B). With increasing concentrations of PdH nanoparticles, intracellular ROS levels gradually elevated, but the levels remained at a consistently low level. Notably, under laser irradiation at the same PdH concentration, LO2 cells exhibited lower ROS levels compared to the non-irradiated condition. This suggests that PdH nanoparticles may exert a protective effect on normal cells by preventing excessive ROS accumulation, thereby reducing the risk of apoptosis.

The cancer cells displayed a completely different ROS response after treatment with PdH as shown in Fig. 12A and 12C-D. Without laser exposure, the addition of PdH nanoparticles caused a moderate increase in ROS in HepG2. When subjected to laser, ROS generation in HepG2 was greatly enhanced at all PdH concentrations. With no PdH (0 μg mL^{-1}), laser alone raised ROS levels, reflecting photothermal stress. As the concentration of PdH increases, the ROS levels rise significantly. At 150 μg mL^{-1} of PdH combined with laser irradiation, the quantified ROS levels in HepG2 cells increased by 5.08-fold compared with the blank control group. Similarly, the quantified ROS levels for SMMC-7721 cells increased by 3.10-fold compared with the blank control group at the same condition (Fig. 12D). The data demonstrate that the thermo-hydrogen therapy induced a substantial oxidative burst in cancer cells, and this elevation of ROS is a likely driver of the enhanced cell

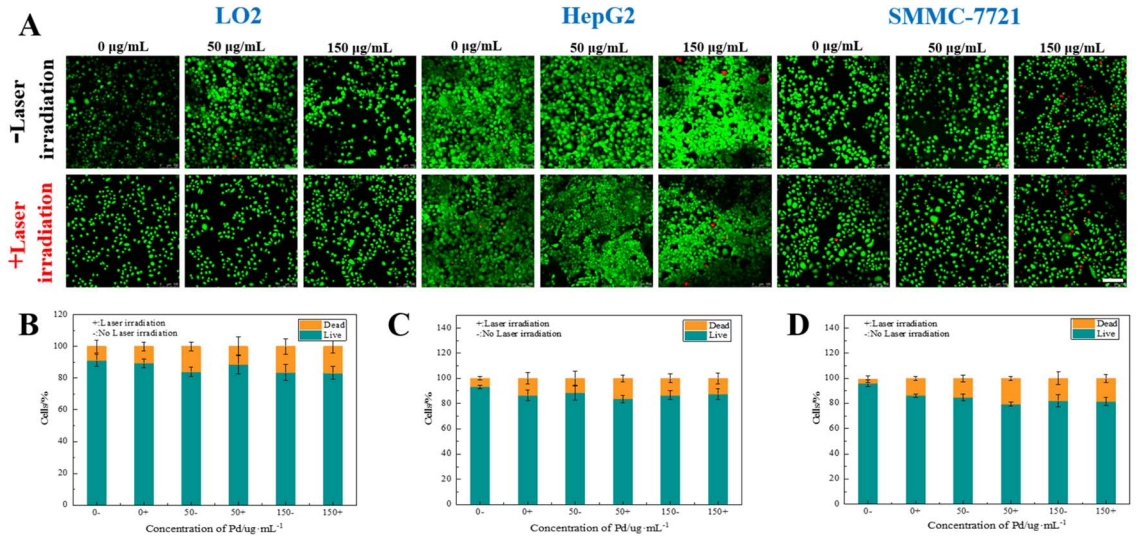

Fig. 10 Live/dead cell staining results of three types of cells under different conditions using Pd nanoparticles. (A) Fluorescence images of human liver cells and liver cancer cells treated with different concentrations of Pd with or without 532 nm laser irradiation (Scale = 100 μm); (B–D) quantification results of green/red fluorescence for LO2 cells, HepG2 cells and SMMC-7721 cells at different Pd concentrations. The data are shown as mean SD (n = 3).

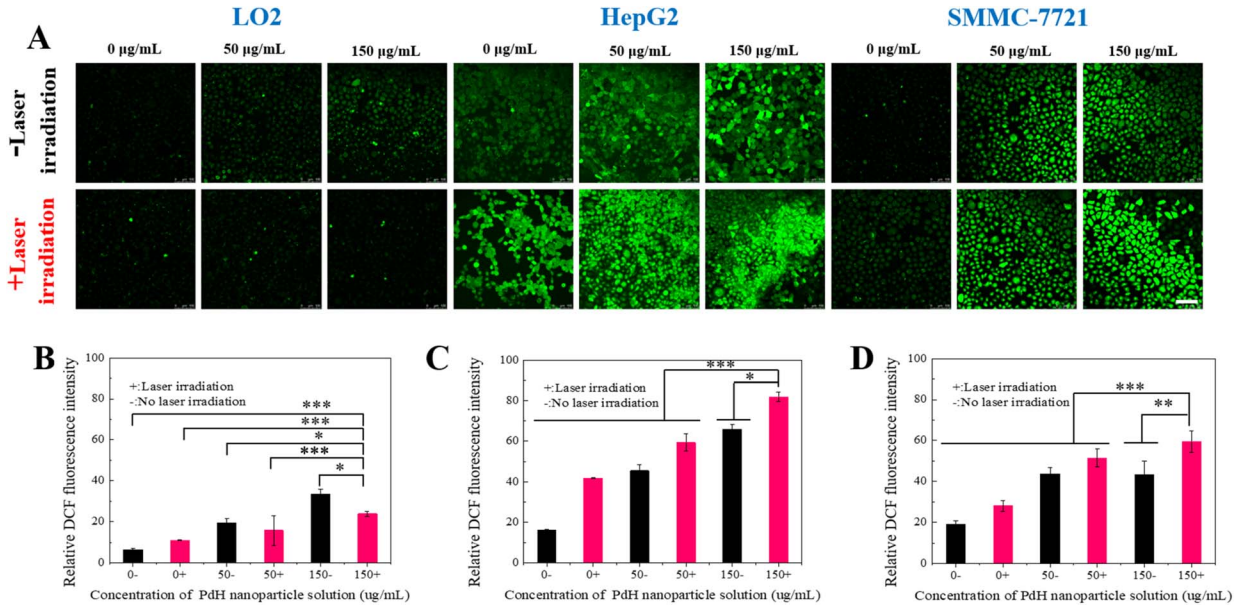

Fig. 11 ROS staining results for three types of cells under different concentrations of PdH nanoparticles. (A) ROS fluorescence images of human liver cells and liver cancer cells with or without 532 nm laser irradiation (Scale = 100 μm); (B–D) quantification results of ROS levels in LO2 cells, HepG2 cells and SMMC-7721 cells, respectively at different PdH concentrations. The data are shown as mean SD (n = 3).

killing. In fact, excess ROS production can disrupt the redox homeostasis, leading to cell death.

To better understand the role of hydrogen, we also compared ROS generation in cells with Pd treatment. As shown in Fig. 12A and B, intracellular ROS in LO2 cells increases with rising Pd concentration, and laser irradiation further augments ROS production. The same trend is observed in both HepG2 cells and SMMC-7721 liver cancer cell lines. However, when treated with Pd nanoparticles, LO2 cells display markedly higher ROS levels than those treated with PdH nanoparticles. Moreover, both HepG2 and SMMC-7721 cancer cells exhibit lower ROS levels after Pd treatment than their PdH treated counterparts. Taken together with the results in Fig. 11 and 12, these findings demonstrate a dual advantage of PdH nanoparticles: (i) they selectively suppress ROS accumulation in normal hepatocytes, thereby preventing oxidative stress-induced apoptosis, and (ii)

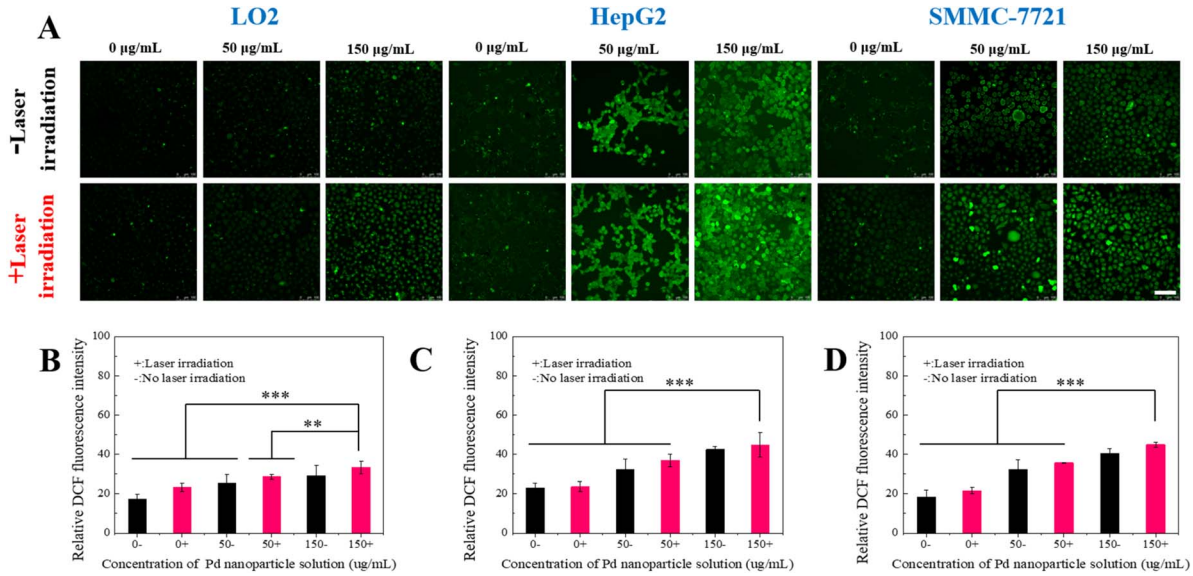

Fig. 12 ROS staining results and quantified results for the three types of cells. (A) Effects of different concentrations of Pd nanoparticles on ROS levels in human liver cells and liver cancer cells under 532 nm light irradiation or without irradiation (Scale = 100 μm); (B) quantification results of ROS levels in LO2 cells at different Pd concentrations; (C) quantification results of ROS levels in HepG2 cells at different Pd concentrations; (D) quantification results of ROS levels in SMMC-7721 cells at different Pd concentrations. The data are shown as mean SD (n = 3).

they markedly elevate oxidative stress in cancer cells, triggering widespread apoptosis and achieving potent cytotoxicity, an outcome unattainable with Pd nanoparticles alone. We noticed a mitochondrial disruption in both cancer cell lines (Fig. S1), which indicated that the markedly elevated oxidative stress observed in cancer cells may be associated with cell-type-dependent redox perturbation under thermo-hydrogen treatment.[17] An in-depth investigation is further needed to understand the underlying anticancer mechanisms.

Recent advances also imply that the acidic microenvironment characteristic of tumor tissues can further promote the release of H_2,[28] leading to enhanced therapeutic efficacy. These observations provide further evidence for the superior efficacy of the Thermo-hydrogen coupling therapeutic strategy. Compared with previously reported Thermo-Hydrogen therapies, the hydrogen-loading platform employed in this study features a significantly simplified fabrication process, eliminating the need for complex multi-material modifications.[29] Overall, this therapeutic strategy demonstrates strong potential for future biomedical applications.

4. Conclusions

In summary, this study presents a PdH nanoparticle platform that achieves synergistic enhancement of oxidative stress in tumor cells through thermo-hydrogen coupling. The synthesized PdH nanoparticles showed high photothermal conversion efficiency and demonstrated stability under prolonged laser irradiation. Hydrogen release experiments indicated that PdH nanoparticles could controllably release hydrogen at temperatures below 60 °C, staying within the biological damage threshold. The PdH nanoparticles exhibit strong biocompatibility to normal or cancerous liver cells in the absence of laser irradiation. However, under laser exposure, PdH significantly increased reactive oxygen species (ROS) levels in cancer cells, inducing apoptosis, while maintaining stable ROS levels in normal cells. The oxidative stress in cancer cells was elevated, resulting in an 82% cancer cell mortality rate. Meanwhile, cell experiments using Pd nanoparticles alone demonstrated limited protective effect to normal hepatocytes and failed to exert effective cytotoxicity against liver cancer cells. These findings suggest a controlled and selective therapeutic approach that minimizes off-target effects by PdH nanomaterials, offering a foundation for further exploration in preclinical models.

Conflicts of interest

There are no conflicts to declare.

Data availability

The data supporting the findings of this study are available within the article and its supplementary information (SI). Supplementary information is available. See DOI: https://doi.org/10.1039/d6ra02688e.

Acknowledgements

This work is supported by the National Natural Science Foundation of China (No. 52276084), Key Research and Development Program of Shaanxi (2024QY2-GJHX-41) and the Recruitment of Overseas High-level Talents Program of Xi'an (24HWYZ0049).

Notes and references

1 L. Peraldo Bicelli, *Int. J. Hydrogen Energy*, 1986, **11**, 555–562.
2 I. P. Jain, *Int. J. Hydrogen Energy*, 2009, **34**, 7368–7378.
3 I. Ohsawa, M. Ishikawa, K. Takahashi, *et al.*, *Nat. Med.*, 2007, **13**, 688–694.
4 Y. Chen and L. Feng, *Sichuan Med. J.*, 2008, **7**, 844–846.
5 J. Zhang and X. Yu, *Chin. J. Pract. Med.*, 2001, **3**, 14–16.
6 G. Zhou, Y. Wang and Z. Jin, *Nanoscale Horiz.*, 2019, **4**, 1185.
7 X. Kong, T. Lu, Y. Y. Lu, *et al.*, *Front. Med.*, 2022, **9**, 828370.
8 Q. Yang, G. Ji, R. Pan, *et al.*, *Mol. Clin. Oncol.*, 2017, **7**, 891–896.
9 Y. Saitoh, H. Okayasu, X. Li, *et al.*, *Oncol. Res.*, 2008, **17**, 247–255.
10 H. Akiba, M. Kofu, H. Kobayashi, H. Kitagawa, K. Ikeda, T. Otomo, *et al.*, *J. Am. Chem. Soc.*, 2016, **138**(32), 10238–10243.
11 S. S. Setayandeh, T. Gould, A. Vaez, K. McLennan, N. Armanet and E. Gray, *J. Alloys Compd.*, 2021, **864**, 158713.
12 D. M. Benson, C. F. Tsang, J. D. Sugar, K. Jagannathan, D. B. Robinson, F. El Gabaly, *et al.*, *ACS Appl. Mater. Interfaces*, 2017, **9**(21), 18338–18345.
13 G. Yuan, J. Cen, J. Liao, Y. Huang and L. Jie, *Nanoscale*, 2021, **13**(37), 15576–15589.
14 R. S. Sherbo, M. Moreno-Gonzalez, N. J. J. Johnson, D. J. Dvorak, D. K. Fork and C. P. Berlinguette, *Chem. Mater.*, 2018, **30**(12), 3963–3970.
15 Y. Nanba, T. Tsutsumi, T. Ishimoto and M. Koyama, *J. Phys. Chem. C*, 2017, **121**(27), 14611–14617.
16 C. M. Ghimbeu, C. Zlotea, R. Gadiou, F. Cuevas, E. Leroy, M. Latroche, *et al.*, *J. Mater. Chem.*, 2011, **21**(44), 17765–17775.
17 P. Zhao, Z. Jin, Q. Chen, T. Yang, D. Chen, J. Meng, *et al.*, *Nat. Commun.*, 2018, **9**, 4241.
18 S. Shi, Y. Huang, X. Chen, J. Weng and N. Zheng, *ACS Appl. Mater. Interfaces*, 2015, **7**, 14369–14375.
19 S. Tang, M. Chen and N. Zheng, *Nano Res.*, 2015, **8**, 165–174.
20 J. Li, H. Liu, J. Ming, D. Sun, X. Chen, X. Liu and N. Zheng, *Chem. Sci.*, 2019, **10**, 1677–1686.
21 N. Joudeh, A. Saragliadis, G. Koster, P. Mikheenko and D. Linke, *Front. Nanotechnol.*, 2022, **4**, 1062608.
22 J. R. Melamed, R. S. Edelstein and E. S. Day, *ACS Nano*, 2015, **9**, 6–11.
23 R. K. Pathak, S. Marrache, J. H. Choi, T. B. Berding and S. Dhar, *Angew. Chem., Int. Ed.*, 2014, **53**, 1963–1967.
24 D. Roper, W. Keith Ahn and M. Hoepfner, *J. Phys. Chem. C*, 2007, **111**(9), 3636–3641.
25 H. Chen, B. Ding, J. Tan, *et al.*, *Chem. Eng. J.*, 2022, **442**, 136296.

26 W. Liu, Z. DD, S. Lin, *et al.*, *RSC Adv.*, 2016, **6**(19), 15854–15860.
27 Q. Dong, X. Wang, X. Hu, L. Xiao, L. Zhang, L. Song, M. Xu, Y. Zou, L. Chen, Z. Chen and W. Tan, *Angew. Chem., Int. Ed.*, 2018, **57**, 177–181.
28 J. Gao, M. Wang, Y. Wang, *et al.*, *Adv. Healthcare Mater.*, 2024, **13**, 2401060.
29 C. Zhang, D. W. Zheng, C. X. Li, *et al.*, *Biomaterials*, 2019, **223**, 119472.
30 Z. Kou, P. Zhao, Z. Wang, *et al.*, *J. Mater. Chem. B*, 2019, **7**(17), 2759–2765.
31 J. W. Xiao, S. X. Fan, F. Wang, *et al.*, *Nanoscale*, 2014, **6**(8), 4345–4351.
32 B. Z, L. He, C. Gong, *et al.*, *Int. J. Hydrogen Energy*, 2019, **44**(3), 1525–1533.
33 B. Z, H. Peng, L. Yang, *et al.*, *J. Mater. Chem. A*, 2015, **3**(3), 973–977.
34 L. Fu, D. Li, L. Peng, *et al.*, *Surf. Interfaces*, 2023, **42**, 103503.